THEORETICAL ANALYSIS OF ELECTROSTATIC ENERGY HARVESTER CONFIGURED AS BENNET'S DOUBLER BASED ON Q–V CYCLES

Binh Duc Truong, Cuong Phu Le and Einar Halvorsen

Keywords: *Q–V cycle, Bennet's doubler, saturation voltage, electrostatic energy harvester.*

Abstract – We present a theoretical analysis of a MEMS electrostatic energy harvester configured as Bennet's doubler. The steady–state operation of the circuit can be approximated by a rectangular Q–V cycle in the ideal case or by a trapezoid diagram when the electrical losses are taken into account. A similarity between the voltage doubler and charge–pump circuit is highlighted. The analytical solution of the saturation voltage is derived, providing a more insightful comprehension of the system performance and the influence of its parameters. The results obtained from studying the Q–V diagram coincide with those of circuit simulations for both cases when using (i) a mathematically idealized diode or (ii) a realistic diode model that includes the electrical losses. Voltage multiplier circuits with different topologies that can further increase the saturation voltage are investigated, providing various alternatives for boosting the output voltage of an electrostatic energy harvester when needed.

1. INTRODUCTION

Wireless sensor nodes (WSNs) are emerging as one of the most commonly used systems for monitoring and sensing applications [1,2]. Most current WSNs are powered by batteries. The lifetime of batteries is limited to a few years, and improper disposal of batteries could pose a significant threat to human health and the environment. Energy harvesting from vibration has become a potential alternative to obtain electrical energy for WSNs, especially in some circumstances where batteries may not be feasible due to size constraints. For the vibration energy harvesters, there are three common transduction mechanisms which includes piezoelectric, electromagnetic and electrostatic [3–5]. In this paper, we focus on an overlap–varying electrostatic energy harvesting system.

A challenge with energy harvesters is the implementation of power management circuits due to the limited power available in the generators. In an early effort, Roundy *et al.* introduced a simple charge pump circuit consisting of a voltage source, an electrostatic converter, and two switches and demonstrated that mechanical–to–electrical energy transduction based on variable capacitance is possible [6]. When connected to a load resistance, the correlation between the charge and voltage of the variable capacitor can be described by a Q–V cycle of a triangular shape [7]. However, the authors did not consider the regime where the generator saturates due to the lack of an energy flyback path.

In order to overcome this issue, several solutions based on energy–renewal techniques for extracting electrical energy were investigated. For instance, Yen *et al.* proposed a configuration of single variable–capacitance harvester, combining an asynchronous charge pump with an inductive flyback circuit to recharge a scavenging capacitor [8]. Mitcheson *et al.* developed a buck–boost topology with bi–directional switches for rectifying and increasing the AC voltage obtained from electromagnetic, electrostatic and piezoelectric transducers [9]. However, these circuit topologies face the challenges of power consumption of the control unit and harvester efficiency.

Bennet's doubler of electricity was introduced already in 1787 by Bennet and Kaye [10]. A macro–scale device with three plates is used to continuously double a small initial charge through a sequence of operations. Based on this approach, de Queiroz proposed a promising variation of such a voltage doubler for vibration energy harvesters composed of variable capacitors and diodes replacing switches [11–13]. In order to adapt this concept to micro–scale electrostatic generators, several studies have been made [14–20], including attempts to increase the charging current for a reservoir capacitor or to optimize the harvested power. In a recent work by Galayko [21], operation of the doubler configuration with a single variable capacitor was thoroughly analyzed in the electrical domain.

With ideal diodes (i.e., zero forward voltage and no leakage current), a rectangular conversion cycle can be realized to investigate the performance of Bennet's doubler. A complete model was developed, taking the dynamics of the mechanical domain into account [22, 23]. When delivering energy into a storage capacitor, higher voltages induce more electrical damping in the transducers. As a consequence, the steady–state operation of the harvesting system is achieved, and the output voltage saturates at a certain level. However, the operation of a transducer configuration with two time–varying capacitors and closed forms of the saturated voltage (denoted as V_s) has not been explored yet.

The saturation phenomenon was observed in both simulation and experiment [16,19]. Therefore, the effect of electromechanical coupling on it is of interest to comprehensively investigate. This paper further presents a theoretical analysis of Bennet's doubler circuit based on the Q–V cycle. In particular, the explicit dependence of V_s on input acceleration and harvester parameters is the central objective. Non-ideal effect of diodes on the shape of the Q-V diagram is also an important objective. A complete model of an anti–phase overlap–varying transducer electrically configured as a voltage doubler is investigated. Numerical results for both ideal- and non-ideal diodes obtained by a circuit simulator are used to verify the analytical solutions. In order to further increase the saturated voltage across the storage capacitor, alternative topologies are introduced and analyzed.

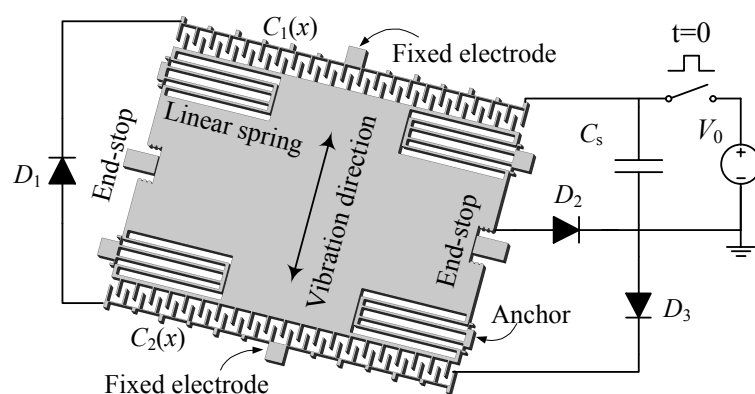## 2. Steady state operation with mathematically idealized diodes

FIGURE 1. Overlap–varying energy harvesters employing Bennet's doubler circuit.

2.1. **Theoretical analysis.** Overlap–varying energy harvesters can be utilized in a charge–doubling circuit–configuration as shown in Figure 1 [14,19]. The transducer capacitors are precharged to a voltage V_0. At time $t = 0$, the switch connecting the voltage source V_0 with the harvester is turned off. The proof mass is suspended by four folded–beam linear springs. The maximum displacement

$X_{\max}$ is defined by mechanical end–stops. Two anti-phase variable capacitors $C_{1/2}(x) = C_0(1 \pm \frac{x}{x_0})$ are connected to three diodes D_1, D_2, D_3 and the storage capacitor C_s. Here C_0, x_0 and x are the nominal capacitance, the nominal overlap and the proof mass displacement, respectively. Operation of the doubler circuit does not require any control unit or switches but an initial bias voltage V_0.
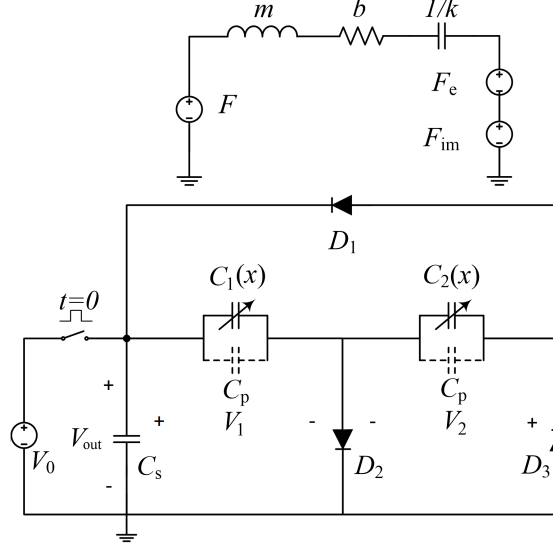

FIGURE 2. Equivalent circuit for mechanical domain and Bennet's doubler configuration.

Figure 2 shows a complete lumped model of the doubler configuration, including an equivalent circuit for the mechanical subsystem. where m - proof mass, b - mechanical damping, k - total spring stiffness, F - external force, F_e - electrostatic force and C_p - parasitic capacitance of each transducer. The impact force F_{im} acting on the proof mass when the displacement reach its maximum is simply modeled as a spring–damper system. In particular, $F_{im} = k_{im}\delta + b_{im}\dot{\delta}$ for $|x| \geq X_{\max}$ [24], where $\delta = |x| - X_{\max}$ is relative displacement between the proof mass and the end–stops, k_{im} is the impact stiffness, and b_{im} is the impact damping. The vibration frequency is chosen as $f = f_0 = \frac{1}{2\pi}\sqrt{\frac{k}{m}}$. For a sufficient voltage V_0 and an adequate input acceleration amplitude A, the voltage accumulated on the storage capacitor C_s initially increases. Figure 3 indicates that after certain cycles of the transient regime, the harvester attains its steady–state operation. The electrical energy is now no longer scavenged, and the output voltage V_{out} maintains constant at V_s (i.e., saturation voltage).

The proof mass displacement amplitude X_0 changes in a complicated manner. X_0 first reaches the maximum value $X_0 \approx X_{\max}$ (i.e., which is limited by the mechanical end-stops), then decreases and keeps fixed at $X_0 \approx X_s$ in the saturation regime. For convenience, we define the rate of voltage evolution v^* as a ratio of the maximum output voltage in two subsequent period

$$(2.1) \qquad v^* = \frac{\max\left(V_{out}\big|_{T_{i+1}}\right)}{\max\left(V_{out}\big|_{T_i}\right)}.$$

As shown in Figure 3, v^* is modified over cycles under the variation of X_0, as follows. During the transient regime, v^* is small at the beginning and gradually increases, meanwhile $X_0 \approx X_{\max}$. After reaching the maximum, v^* decreases with the reduction of X_0 and finally becomes unity at which the steady state is achieved.
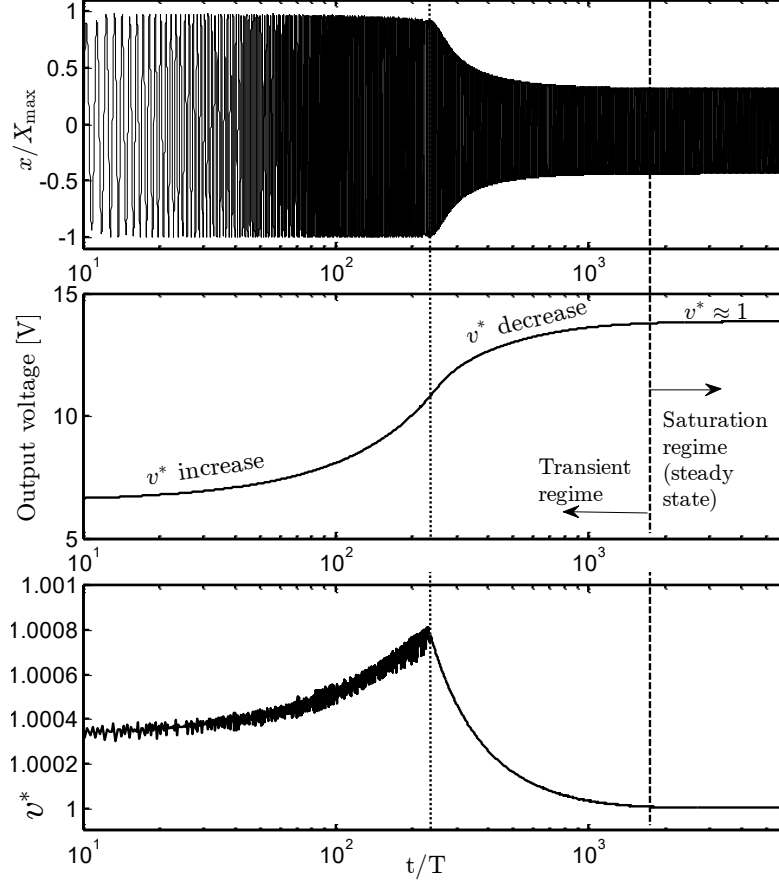
FIGURE 3. Evolution of the proof mass displacement and the output voltage across the storage capacitor with the input acceleration amplitude $A = 2.0$ g, the drive frequency $f = f_0$ and the initial bias voltage $V_0 = 7$ V.

TABLE 1. Model parameters

Parameter	Value
Proof mass, m	1.022 mg
Spring stiffness, k	3.595 N/m
Thin-film air damping, b	3.478e-5 Ns/m
Nominal overlap, x_0	80 μm
Nominal capacitance, C_0	15 pF
Parasitic capacitance, C_p	7.5 pF
Storage capacitance, C_s	10 nF
Contact stiffness, k_{im}	3.361 MN/m
Impact damping, b_{im}	0.435 Ns/m
Maximum displacement, X_{max}	80 μm

The higher voltages through the conversion phase, the more effective electrical damping (represented by electrostatic force) is induced in the transducers, causing a decrease in the proof mass displacement. As a consequence, the transducer capacitance ratio $\eta = (C_{max} + C_p)/(C_{min} + C_p)$ is reduced. Here, $C_{max} = C_0(1 + X_s/x_0)$, $C_{min} = C_0(1 - X_s/x_0)$, and $X_s < X_{max}$ is the displacement

amplitude at saturation. With the model parameters taken from [19] and listed in Table 1, we have $\eta \approx 1.72$. It is important to note that the necessary condition for the operation of the doubler circuit is $\eta \geq \eta_{cr} = 2$, where η_{cr} is the critical threshold ratio in the ideal case (i.e., without any losses) [11]. Since this condition is no longer satisfied, V_{out} is saturated at V_s. In this paper, the effect of the electromechanical coupling on the solution of V_s through the impact of the electrostatic force is one of the primary objectives of the analytical investigation.

Figure 4 shows the waveform of the proof mass displacement, the voltages V_1, V_2 across C_1, C_2, and the currents I_{D1}, I_{D2}, I_{D3} through three mathematically idealized diodes, respectively. Dynamic simulations are performed by using LTspice simulator. The operation of the doubler circuit at the steady–state operation is divided into a sequence of four stages from t_0 to t_4. We observe that the relation of Q_1 and V_1 now can be approximated by a rectangular Q–V cycle diagram since the time interval between $\Delta t_{21} = t_2 - t_1$ and $\Delta t_{43} = t_4 - t_3$ are negligibly small. We now consider
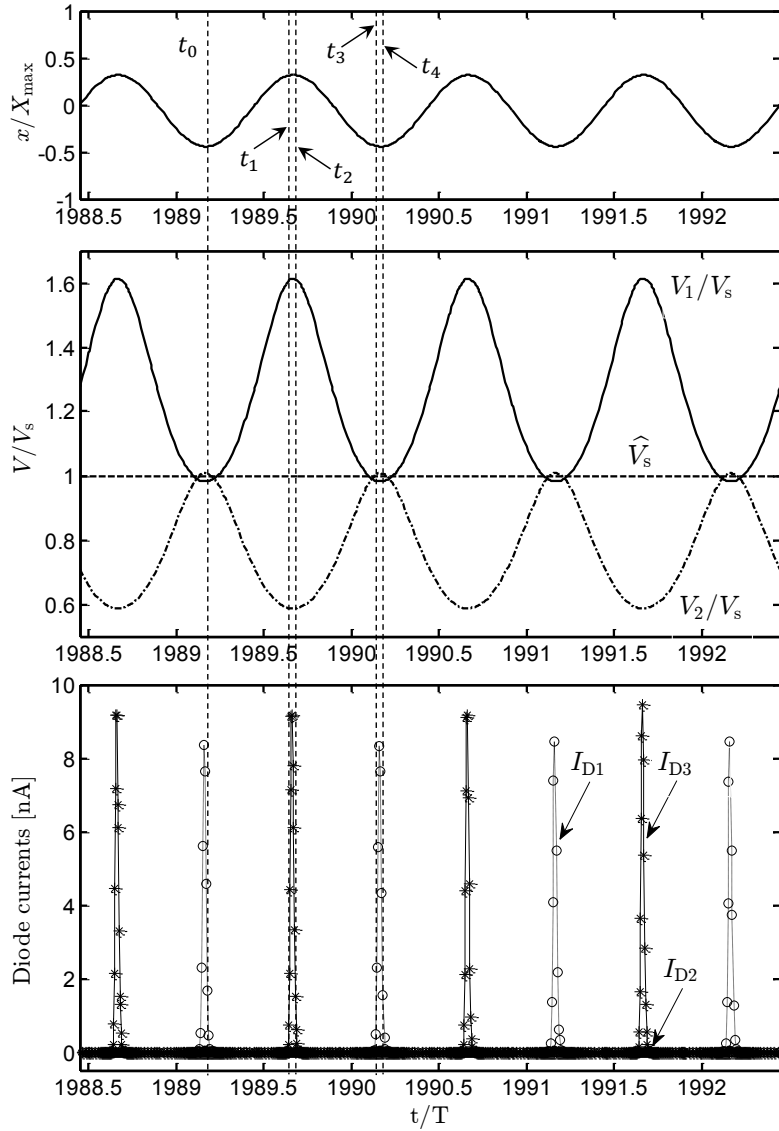

FIGURE 4. Waveforms of displacement, voltages on variable capacitors and currents through three diodes at steady state with $A = 2.0$ g and $f = f_0$.
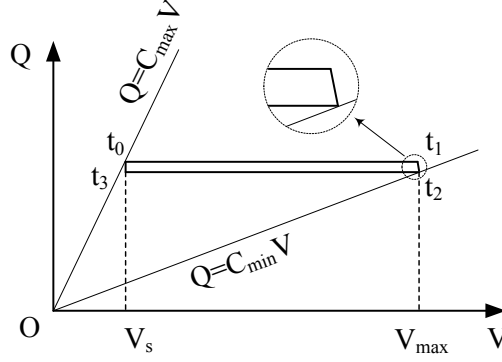
FIGURE 5. Approximated Q–V diagram of variable capacitor $C_1(x)$ at steady state with mathematically ideal diodes.

each of the four stages in turn, as depicted in Figure 5, and *all the following computations are based on the Q–V diagram only.*

Stage I: At $t = t_0$, $x(t_0) = -X_s$ and $V_1(t_0) \approx V_2(t_0) \approx V_s$, where X_s is the maximum displacement at the steady–state. From t_0 to t_1, all three diodes D_1, D_2 and D_3 are blocked as the condition $V_{C_2} < V_s < V_{C_1} < V_{C_2} + V_s$ is satisfied. The charges on the two transducers are

$$q_1(t_0) = V_s\Big[C_p + C_0(1 + \frac{X_s}{x_0})\Big], \tag{2.2}$$

$$q_2(t_0) = V_s\Big[C_p + C_0(1 - \frac{X_s}{x_0})\Big]. \tag{2.3}$$

In the first stage, q_1 and q_2 are constants, V_1 and V_2 are given

$$V_1\Big|_{t\in[t_0, t_1]} = \frac{q_1}{C_1} = \frac{V_s\Big[C_p + C_0(1 + \frac{X_s}{x_0})\Big]}{C_p + C_0(1 - \frac{x}{x_0})}, \tag{2.4}$$

$$V_2\Big|_{t\in[t_0, t_1]} = \frac{q_2}{C_2} = \frac{V_s\Big[C_p + C_0(1 - \frac{X_s}{x_0})\Big]}{C_p + C_0(1 + \frac{x}{x_0})}. \tag{2.5}$$

Stage II: At $t = t_1$, $V_1(t_1) \approx V_2(t_1) + V_s$, and diode D_3 starts to conduct. Since the time interval between t_1 and t_2 is very small (i.e., see Figure 5), the proof mass displacement at t_1 can be approximated as $x(t_1) \approx x(t_2) = X_s$, then

$$\frac{1 + \frac{C_0}{C_p}\left(1 + \frac{X_s}{x_0}\right)}{1 + \frac{C_0}{C_p}\left(1 - \frac{X_s}{x_0}\right)} = 1 + \frac{1 + \frac{C_0}{C_p}\left(1 - \frac{X_s}{x_0}\right)}{1 + \frac{C_0}{C_p}\left(1 + \frac{X_s}{x_0}\right)}. \tag{2.6}$$

The solution is given by

$$X_s = \left(\sqrt{5} - 2\right)\left(1 + \frac{C_p}{C_0}\right)x_0. \tag{2.7}$$

The peak values of voltages across C_1 and C_2 are

$$V_I = V_1(t_1) = V_1(t_2) = V_s\frac{\sqrt{5} + 1}{2}, \tag{2.8}$$

$$V_{II} = V_2(t_1) = V_2(t_2) = V_s\frac{\sqrt{5} - 1}{2}. \tag{2.9}$$

In this stage, net charges ΔQ_s and ΔQ are pumped from C_1 into C_s and C_2, respectively. At steady state, V_s is considered unchanged, thus ΔQ_s is neglected. The detailed derivation is presented in Appendix A.

Stage III: From t_2 to t_3, all diodes are blocked, q_1 and q_2 are constants

$$(2.10) \qquad q_1\Big|_{t\in[t_2,\,t_3]} = q_1(t_2) = V_s\Big[C_p + C_0(1 + \frac{X_s}{x_0})\Big] - \Delta Q,$$

$$(2.11) \qquad q_2\Big|_{t\in[t_2,\,t_3]} = q_2(t_2) = V_s\Big[C_p + C_0(1 - \frac{X_s}{x_0})\Big] + \Delta Q.$$

At t_3, $x(t_3) = x_3$ and

$$(2.12) \qquad V_1(t_3) = V_s.$$

Diode D_2 starts to conduct, transferring an amount of charge ΔQ^* from C_s into C_1. Similarly, since V_s is treated as constant, ΔQ^* is thus negligible. The relation (2.12) now can be written as

$$(2.13) \qquad V_1(t_3) = \frac{q_1(t_3)}{C_1(t_3)} = \frac{V_s\Big[C_p + C_0(1 + \frac{X_s}{x_0})\Big] - \Delta Q}{C_p + C_0(1 - \frac{x_3}{x_0})} = V_s.$$

Due to the small interval time between t_3 and t_4, $x_3 \approx x(t_4) = -X_s$, resulting in $\Delta Q \approx 0$. In other words, the charge transfered from C_1 into C_2 is insignificant.

Considering the voltage across the capacitor C_2 at t_3, we have

$$(2.14) \qquad V_2(t_3) = \frac{q_2(t_3)}{C_2(t_3)} = \frac{V_s\Big[C_p + C_0(1 - \frac{X_s}{x_0})\Big] + \Delta Q}{C_p + C_0(1 + \frac{x_3}{x_0})} \approx V_s.$$

Since the condition $V_2 \approx V_s$ holds, D_1 also starts to conduct at t_3 .

Stage IV: From t_3 to t_4, D_1 is conducting, and ΔQ is transfered from C_2 into C_1. The charge $q_1(t_4)$ is

$$(2.15) \qquad q_1(t_4) = q_1(t_3) + \Delta Q = V_s\Big[C_p + C_0(1 + \frac{X_s}{x_0})\Big].$$

The condition $q_1(t_4) = q_1(t_0)$ is fulfilled, showing that the state of the doubler circuit at t_4 is the same as when $t = t_0$. A new cycle then starts. This result proves that the right–angle trapezoid Q–V diagram is capable of describing the operation of the doubler circuit in the case of using idealized or low–loss diodes.

2.2. **Similarity of Bennet'doubler and charge-pump circuit.** Among electronic interface circuits for MEMS capacitive energy harvesters [25,26], the charge pump circuit [6] and its varieties are widely investigated. A well-known charge pump variation that combines with an inductive flyback circuit was developed by Yen *et al.* [8]. An alternative technique to implement flyback is to use a load resistance, which was first introduced in [27] and thoroughly analyzed in [23].

Comparing the results reported in the literature with those obtained in the first sections of this paper, it is worth noting that the Q-V cycle for the charge pump circuit with resistive flyback is very similar to that of Bennet's doubler circuit. Both the charge pump and voltage doubler can be approximated by a rectangular conversion cycle in the ideal circumstance in that the electrical loss is neglected. Furthermore, at the steady–state operation, the Q–V cycle of the two topologies almost degenerates into a line (as seen in Figure 5).
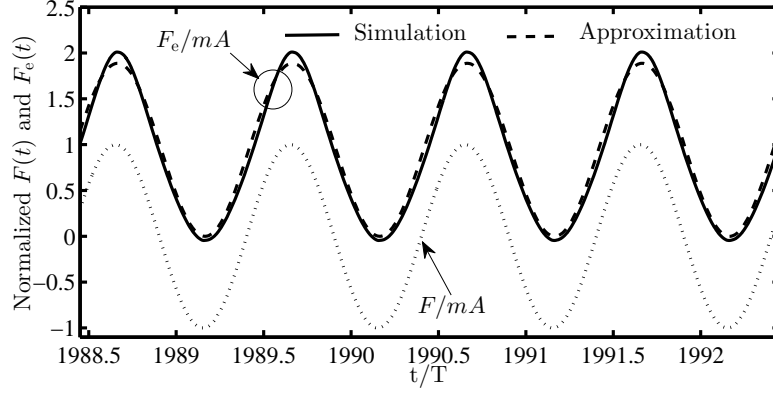
FIGURE 6. Normalized waveforms of the input acceleration in comparison with the electrostatic force obtained from simulation and formula (3.5).

3. APPROXIMATION OF THE SATURATION VOLTAGE WITH MATHEMATICALLY IDEAL DIODE

The electrostatic force F_e plays an essential role in the saturation phenomenon of the output voltage. Therefore, it is the primary objective of the study in this Section. F_e is modeled as

$$(3.1) \qquad F_e = -\frac{1}{2}\frac{\partial C_1(x)}{\partial x}V_1^2 - \frac{1}{2}\frac{\partial C_2(x)}{\partial x}V_2^2 = \frac{1}{2}\frac{C_0}{x_0}\big(V_1^2 - V_2^2\big).$$

V_1 and V_2 can be simplified as anti–phase sinusoidal signals for the sake of analysis, although they are more complicated than that in general. Based on the dynamic simulations, we observe that the phase difference between *the input acceleration* and *the voltage across C_1* is negligibly small and is ignored.

Using expressions (2.8) and (2.9), the waveforms of V_1 and V_2 are then represented as

$$(3.2) \qquad V_1 = \frac{V_I + V_s}{2} + \frac{V_I - V_s}{2}\sin(\omega t) = V_s\frac{3+\sqrt{5}}{4} + V_s\frac{-1+\sqrt{5}}{4}\sin(\omega t),$$

$$(3.3) \qquad V_2 = \frac{V_{II} + V_s}{2} - \frac{V_s - V_{II}}{2}\sin(\omega t) = V_s\frac{1+\sqrt{5}}{4} - V_s\frac{3-\sqrt{5}}{4}\sin(\omega t),$$

yielding

$$(3.4) \qquad V_1^2 - V_2^2 = \frac{2+\sqrt{5}}{4}V_s^2\big(1 + \sin(\omega t)\big)\Big(1 + \frac{(\sqrt{5}-2)^2}{2}\sin(\omega t)\Big).$$

The coefficient $(\sqrt{5}-2)^2/2 \approx 0.028 \ll 1$ is negligible, and the electrostatic force thus becomes

$$(3.5) \qquad F_e = \frac{2+\sqrt{5}}{8}\frac{C_0}{x_0}V_s^2\big(1 + \sin(\omega t)\big) = F_0\big(1 + \sin(\omega t)\big)$$

where

$$(3.6) \qquad F_0 = \frac{2+\sqrt{5}}{8}\frac{C_0}{x_0}V_s^2.$$

The harmonic term of F_e is in phase with the input acceleration. Figure 6 shows the comparison between the input acceleration and the electrostatic force over the same time duration as in Figure 4. The expression of F_e in (3.5) is in good agreement with the wave form obtained by the simulation.

The differential equation of the spring–mass–damping system, which is set in continuous oscillation by a sinusoidal force acting on the proof mass, is

$$(3.7) \qquad m\ddot{x} + b\dot{x} + kx = mA\sin\big(\omega t\big) - F_e.$$

The steady–state solution of (3.7) is $x = -\bar{x} + x_\mathrm{h}$, where $\bar{x} = F_0/k$ is the offset displacement. The harmonic term is [28]

$$(3.8) \qquad x_\mathrm{h} = X_0 \sin(\omega t + \varphi)$$

where

$$(3.9) \qquad X_0 = \frac{(mA - F_0)/m}{\sqrt{\left(\omega^2 - \omega_0^2\right)^2 + \left(\frac{b}{m}\right)^2 \omega^2}}.$$

In the saturation regime, the proof mass displacement does not reach its physical constraint defined by the rigid end–stops, $X_\mathrm{s} < X_\mathrm{max}$. With $\omega = \omega_0 = \sqrt{k/m}$, the peak value of x_h is

$$(3.10) \qquad X_\mathrm{s} = X_0 = \frac{mA - F_0}{b\omega_0}.$$

The ratio $\bar{x}/X_0$ obtained from simulations is less than 2.1% for all $A \in [1, 2]$ g, the acceleration range of interest. Therefore, $\bar{x}$ is assumed negligible, and approximately $x \approx x_\mathrm{h}$. By considering amplitudes of the harmonic term and ignoring phase differences, the saturation voltage is

$$(3.11) \qquad V_\mathrm{s} = \sqrt{\frac{8}{2 + \sqrt{5}} \frac{mA - \left(\sqrt{5} - 2\right)\left(1 + C_\mathrm{p}/C_0\right)x_0 b\omega_0}{C_0/x_0}}.$$

The details of derivation are included in Appendix B.

Although the performance of the harvesting system using a mathematically ideal diode is analyzed, the effects of power loss (due to diode imperfections such as leakage current and junction capacitance) on the shape of the Q–V cycle and the solution of V_s are still open for investigation. This issue is even of greater interest and to be explored in the next section.

4. Operation of the Bennet's Doubler with non–ideal diode

4.1. **Approximated Q–V Cycle at steady state.** A realistic model of diode 1N6263 is chosen to use in LTspice simulation to assess the effects of diode losses on the harvesting system performance, as the magnitude of the reverse current is comparable with the charging current through the storage capacitor, and the zero bias junction capacitance is in the range of transducer nominal capacitance. Other authors, such as Dragunov [14,29], utilized similar diode parameters to estimate the average charging current for a configuration of the doubler circuit based on a single variable–capacitor.

Figure 7 shows waveforms on the same time scale of the proof mass displacement, the voltages V_1, V_2 across and the charges q_1, q_2 on the variable capacitors C_1 and C_2, respectively. Similarly, the operation of the doubler circuit at the steady–state can be divided into a sequence of four stages. However, the time interval between stages is more significant than those when utilizing mathematically idealized diodes. Based on the observation from the simulation, the relation of $Q_1(Q_2)$ and $V_1(V_2)$ is then approximated by a right–angled trapezoid Q–V cycle diagram, as shown in Figure 8.

For the sake of simplicity, the dynamics of the diodes, such as the time evolution of the diode currents, are disregarded in analyzing the Q–V conversion. In addition, *we assume that the effects of diode losses are accounted for and represented in the change of the Q–V cycle from a rectangular to a right–angled trapezoid.* Charges transferred from or into C_s are negligible since the output voltage is unchanged at steady state. Under these assumptions, the following analyses are developed based on the Q–V diagram only. Differentiating from the previous section, the displacements of the proof mass at t_1 and t_3 are still unknown, and the system behavior is more complicated.
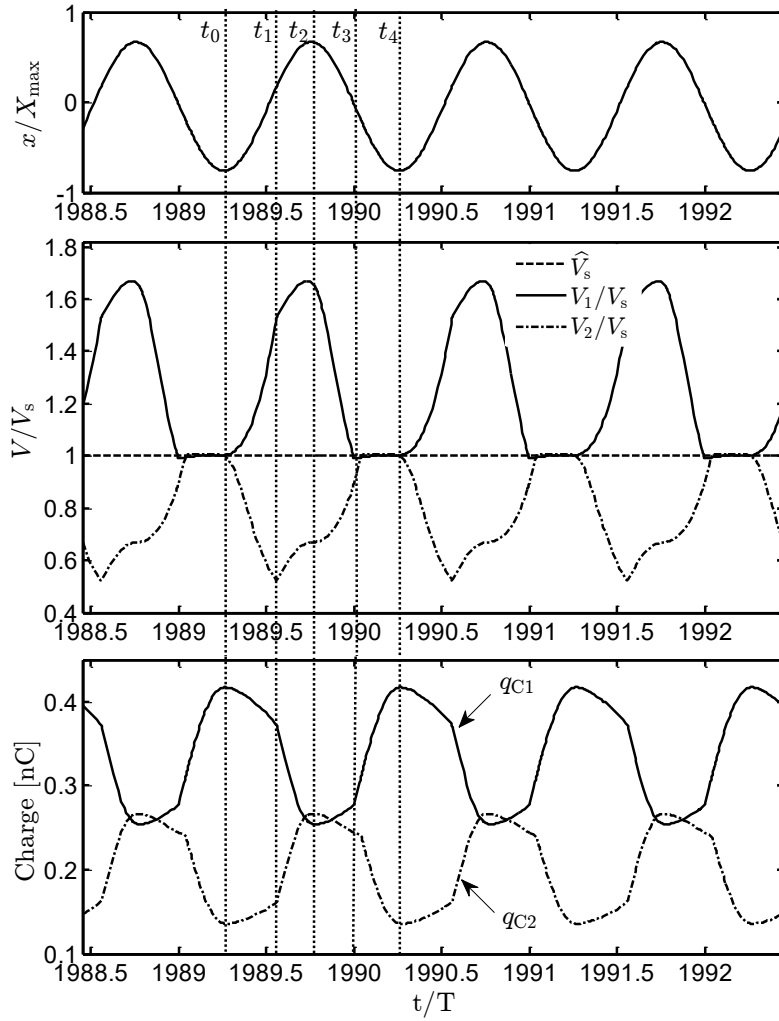
FIGURE 7. Normalized displacement, voltage and charge waveforms on variable capacitors $C_1(x)$ and $C_2(x)$ at saturation with the input external acceleration $A = 2.0$ g.
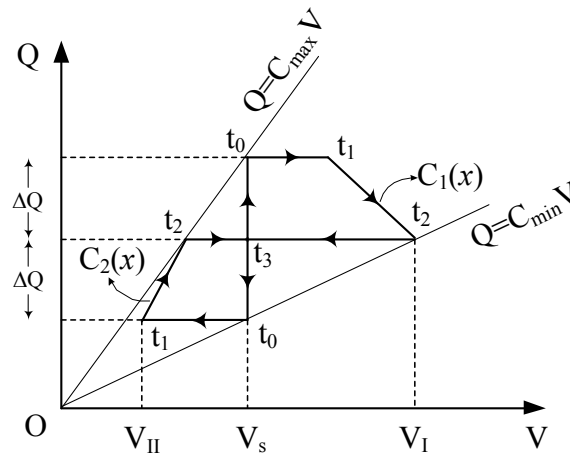

FIGURE 8. Q–V diagram of Bennet's doubler at the steady–state for both variable capacitors.

Stage I: Similar to the previous analysis, the charges on the two generators and variations of V_1 and V_2 from t_0 to t_1 are expressed by equations (2.2), (2.3), (2.4) and (2.5).

Stage II: At $t = t_1$, $x(t_1) = x_1$, $V_1(t_1) = V_2(t_1) + V_s$ and diode D_3 starts to conduct, this yields

$$\text{(4.1)} \qquad \frac{1 + \frac{C_0}{C_p}\left(1 + \frac{X_s}{x_0}\right)}{1 + \frac{C_0}{C_p}\left(1 - \frac{x_1}{x_0}\right)} = 1 + \frac{1 + \frac{C_0}{C_p}\left(1 - \frac{X_s}{x_0}\right)}{1 + \frac{C_0}{C_p}\left(1 + \frac{x_1}{x_0}\right)}.$$

From t_1 to t_2, charge ΔQ is pumped from C_1 into C_2.

Stage III: From t_2 to t_3, all diodes are blocked. Charges q_1 and q_2 are constants that are described by (2.10) and (2.11). At $t = t_3$, D_2 starts to conduct due to $V_1(t_3) = V_s$. This condition is expressed by (2.13), which results in

$$\text{(4.2)} \qquad \Delta Q = V_s C_0 \left(\frac{X_s + x_3}{x_0}\right).$$

The voltage across C_2 at t_3 is

$$\text{(4.3)} \qquad \begin{aligned} V_2(t_3) = \frac{q_2(t_3)}{C_2(t_3)} &= \frac{V_s\left[C_p + C_0(1 - \frac{X_s}{x_0})\right] + \Delta Q}{C_p + C_0(1 + \frac{x_3}{x_0})} \\ &= \frac{V_s\left[C_p + C_0(1 - \frac{X_s}{x_0})\right] + V_s C_0\left(\frac{X_s + x_3}{x_0}\right)}{C_p + C_0(1 + \frac{x_3}{x_0})} = V_s. \end{aligned}$$

Since the condition $V_2 = V_s$ is fulfilled, D_1 also starts to conduct at t_3. Substituting (4.2) into (2.10), we get

$$\text{(4.4)} \qquad q_1(t_3) = V_s\left[C_p + C_0(1 + \frac{x_3}{x_0})\right].$$

Stage IV: From t_3 to t_4, D_1 is conducting and ΔQ is transfered into C_1 from C_2. At t_4, $x(t_4) = -X_s = x(t_0)$ and the state of the doubler circuit is the same as when $t = t_0$, leading to

$$\text{(4.5)} \qquad q_1(t_4) = q_1(t_0)$$

where

$$\text{(4.6)} \qquad q_1(t_4) = q_1(t_3) + \Delta Q = V_s\left[C_p + C_0(1 + \frac{X_s + 2x_3}{x_0})\right].$$

From equations (2.2), (4.5) and (4.6), the displacement at t_3 is given by $x_3 = 0$. As the consequence

$$\text{(4.7)} \qquad \Delta Q = V_s C_0 \frac{X_s}{x_0}.$$

Substituting this result back into (2.10) and (2.11), the voltages across C_1 and C_2 at t_2 are derived as follows

$$\text{(4.8)} \qquad V_1(t_2) = \frac{q_1(t_2)}{C_1(t_2)} = \frac{V_s(C_p + C_0)}{C_p + C_0(1 - \frac{X_s}{x_0})},$$

$$\text{(4.9)} \qquad V_2(t_2) = \frac{q_2(t_2)}{C_2(t_2)} = \frac{V_s(C_p + C_0)}{C_p + C_0(1 + \frac{X_s}{x_0})}.$$

At t_2, D_3 starts to stop conducting since V_1 is slightly less than $V_2 + V_s$. This relation can be approximated as $V_1 \approx V_2 + V_s$. Similarly as equation (4.1), we have

$$\text{(4.10)} \qquad \frac{1 + \frac{C_0}{C_p}}{1 + \frac{C_0}{C_p}\left(1 - \frac{X_s}{x_0}\right)} = 1 + \frac{1 + \frac{C_0}{C_p}}{1 + \frac{C_0}{C_p}\left(1 + \frac{X_s}{x_0}\right)}.$$

The solution of the maximum displacement at the steady–state is

$$(4.11) \qquad X_{\mathrm{s}} = (\sqrt{2} - 1)\left(1 + \frac{C_{\mathrm{p}}}{C_0}\right)x_0.$$

Substituting (4.11) back into (4.1), the proof mass displacement at t_1 is determined by

$$(4.12) \qquad x_1 = \frac{3}{2}\left(\sqrt{4 - 2\sqrt{2}} - 1\right)x_0.$$

Therefore, the peak values of V_1 and V_2 are

$$(4.13) \qquad V_{\mathrm{I}} = V_1(t_2) = V_{\mathrm{s}}\left(1 + \frac{1}{\sqrt{2}}\right),$$

$$(4.14) \qquad V_{\mathrm{II}} = V_2(t_1) = V_{\mathrm{s}}\sqrt{1 - \frac{1}{\sqrt{2}}}.$$

V_1 and V_2 are then approximated by

$$(4.15) \qquad V_1 = \frac{V_{\mathrm{I}} + V_{\mathrm{s}}}{2} + \frac{V_{\mathrm{I}} - V_{\mathrm{s}}}{2}\sin(\omega t) = V_{\mathrm{s}}(1 + \frac{1}{2\sqrt{2}}) + V_{\mathrm{s}}\frac{1}{2\sqrt{2}}\sin(\omega t),$$

$$(4.16) \qquad V_2 = \frac{V_{\mathrm{II}} + V_{\mathrm{s}}}{2} - \frac{V_{\mathrm{s}} - V_{\mathrm{II}}}{2}\sin(\omega t) = V_{\mathrm{s}}\frac{1 + \sqrt{1 - \frac{1}{\sqrt{2}}}}{2} - V_{\mathrm{s}}\frac{1 - \sqrt{1 - \frac{1}{\sqrt{2}}}}{2}\sin(\omega t),$$

yielding

$$(4.17) \qquad V_1^2 - V_2^2 = V_{\mathrm{s}}^2(\alpha + \gamma)\left[(\alpha - \gamma) + (\beta + \lambda)\sin\left(\omega t\right)\right]\left(1 + \frac{\beta - \lambda}{\alpha + \gamma}\sin\left(\omega t\right)\right)$$

where

$$(4.18) \qquad \alpha = 1 + \frac{1}{2\sqrt{2}}, \ \beta = \frac{1}{2\sqrt{2}}, \ \gamma = \frac{1 + \sqrt{1 - \frac{1}{\sqrt{2}}}}{2}, \ \lambda = \frac{1 - \sqrt{1 - \frac{1}{\sqrt{2}}}}{2}.$$

Since $\frac{\beta - \lambda}{\alpha + \gamma} \approx 0.058 \ll 1$ is negligible and $\alpha - \gamma = \beta + \lambda$, the electrostatic force is given by

$$(4.19) \qquad F_{\mathrm{e}} = \frac{1}{2}\frac{C_0}{x_0}V_{\mathrm{s}}^2(\alpha^2 - \gamma^2)(1 + \sin(\omega t)) = \frac{1}{2}\frac{C_0}{x_0}V_{\mathrm{s}}^2\frac{5(1 + \sqrt{2}) - 2\sqrt{4 - 2\sqrt{2}}}{8}(1 + \sin(\omega t)),$$

which can be represented as

$$(4.20) \qquad F_{\mathrm{e}} = F_0(1 + \sin(\omega t))$$

where

$$(4.21) \qquad F_0 = \frac{5(1 + \sqrt{2}) - 2\sqrt{4 - 2\sqrt{2}}}{16}\frac{C_0}{x_0}V_{\mathrm{s}}^2.$$

Using the same analysis procedure in the previous section, the saturation voltage is

$$(4.22) \qquad \begin{aligned} V_{\mathrm{s}} &= \sqrt{\frac{16}{5(1 + \sqrt{2}) - 2\sqrt{4 - 2\sqrt{2}}}\frac{mA - (\sqrt{2} - 1)(1 + \frac{C_{\mathrm{p}}}{C_0})x_0 b\omega_0}{\frac{C_0}{x_0}}} \\ &\approx \sqrt{1.61\frac{mA - (\sqrt{2} - 1)(1 + \frac{C_{\mathrm{p}}}{C_0})x_0 b\omega_0}{\frac{C_0}{x_0}}}. \end{aligned}$$

All the algebraic calculations in this section are presented in Appendix C. Both expressions (3.11) and (4.22) provide a quick means to predict the saturation voltage for any acceleration amplitude and harvester parameters. They can also be utilized as guidelines for designing the overlap-varying anti-phase transducers in order to obtain the desired value of V_{s}.

The ratio between the two solutions of V_s corresponding to the ideal and realistic cases is

$$(4.23) \qquad V_\mathrm{s}^\mathrm{r} = \frac{V_\mathrm{s}^\mathrm{ideal}}{V_\mathrm{s}^\mathrm{non-ideal}} \approx \sqrt{1.17 \frac{mA - (\sqrt{5} - 2)(1 + \frac{C_\mathrm{p}}{C_0})x_0 b\omega_0}{mA - (\sqrt{2} - 1)(1 + \frac{C_\mathrm{p}}{C_0})x_0 b\omega_0}}.$$

Since $(\sqrt{5} - 2) < (\sqrt{2} - 1)$, it is obvious that $V_\mathrm{s}^\mathrm{r} > 1$. Although the diode parameters do not appear in the latter solution of V_s (which follows the assumptions that we made at the beginning of Section 4.1), expression (4.22) still coincides with the fact that diode losses reduce the saturation voltage. In order to verify the accuracy of the analytical results, a comparison with SPICE simulations is to be performed and presented in the following section.
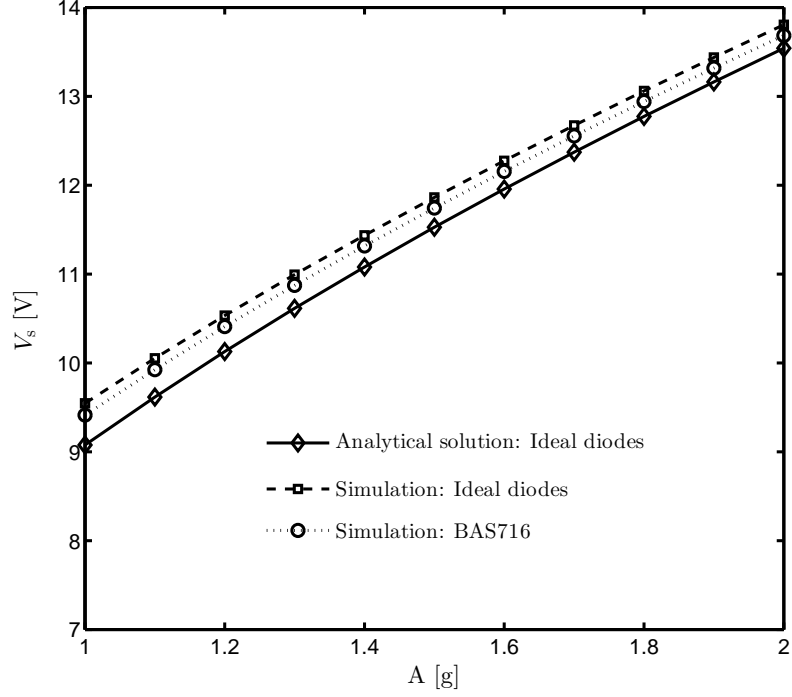
(A) Ideal/Low-losses diode
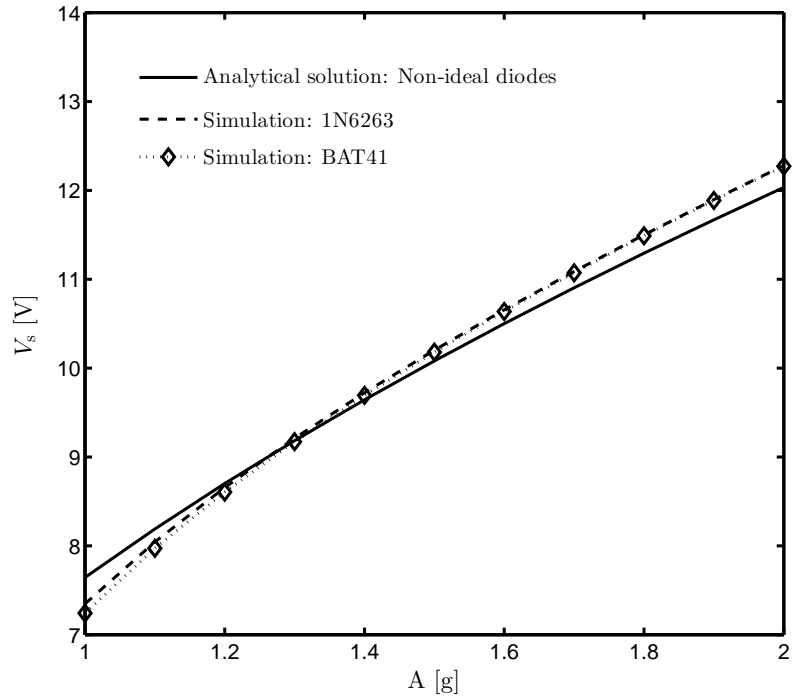
(B) Realistic diode models

FIGURE 9. Acceleration responses of output voltages at steady state: a comparison between simulations and analytical solutions.

4.2. **Numerical verification.** Figure 9a shows the saturation voltage with different acceleration amplitudes. The simulation results that use idealized diodes and those obtained by analytical solution (3.11) are compared. The figure also exhibits that low–loss diode such as BAS716 performs

TABLE 2. Diodes parameters: reverse saturation current I_s, zero-bias junction capacitance C_j and built-in junction voltage V_j

Diode	I_s [nA]	C_j [pF]	V_j [V]
1N6263	3.87	1.77	0.39
BAS716	3.52e-6	1.82	0.65
BAT41	10.00	5.76	0.37
BAT54LPS	20.90	10.60	0.39

close to that of the mathematically idealized diode. In the same manner, Figure 9b presents the analytical solution given by (4.22) compared against the numerical simulations with the use of different non-ideal diode models. Despite disparities in the reverse current I_s, the junction capacitance C_j, and the built–in junction voltage V_j, both diodes 1N6263 and BAT41 give almost the same saturation voltages. The agreement between theoretical and numerical results in both cases verifies our approach and the predictions of the analytical solutions.

The simulations also show that diodes with very high reverse current and large junction capacitance, e.g., BAT54LPS, cause the average charging current through the storage capacitor C_s to be negative, which leads to the discharge of C_s and drop of V_{out} to zero (not shown in the Figure). Those diodes, therefore, are not of interest for doubler configuration. Diode parameters used in the simulations are listed in Table 2. All simulation results are obtained from the LTspice.

4.3. **Effect of diode operation on mechanical dynamics.** The Q–V cycle is a useful geometrical tool that enables us to realize the operation of the voltage doubler circuit at the steady-state. However, the performance of a harvesting system is more sophisticated in the transient regime. Therefore, considering a dynamic simulation may be more appropriate to explore the system behavior.

Figure 10a shows waveforms of the normalized proof mass displacement ($x/X_{\max}$), the normalized external force $\widehat{a} = \sin(\omega t)$, and the electrostatic force (F_{e}/mA) along with the diode currents at the first several operating cycles, utilizing ideal diodes. We observe that the phases of F, x, and F_{e} are initially different. However, those differences gradually decrease due to the effects of the diode states (i.e., blocking and conducting). This phenomenon is most clearly present in the shift of phase of the electrostatic force. Examples of such behavior are marked by the vertical dash lines in the same Figure. This variation process leads to the negligible phase shift between F and F_{e} at the steady–state that we presented in Section 3 and allows us to describe the electrostatic force as the form $F_{\mathrm{e}} = F_0(1 + \sin(\omega t))$. In other words, the dynamic motion of the proof mass also strongly
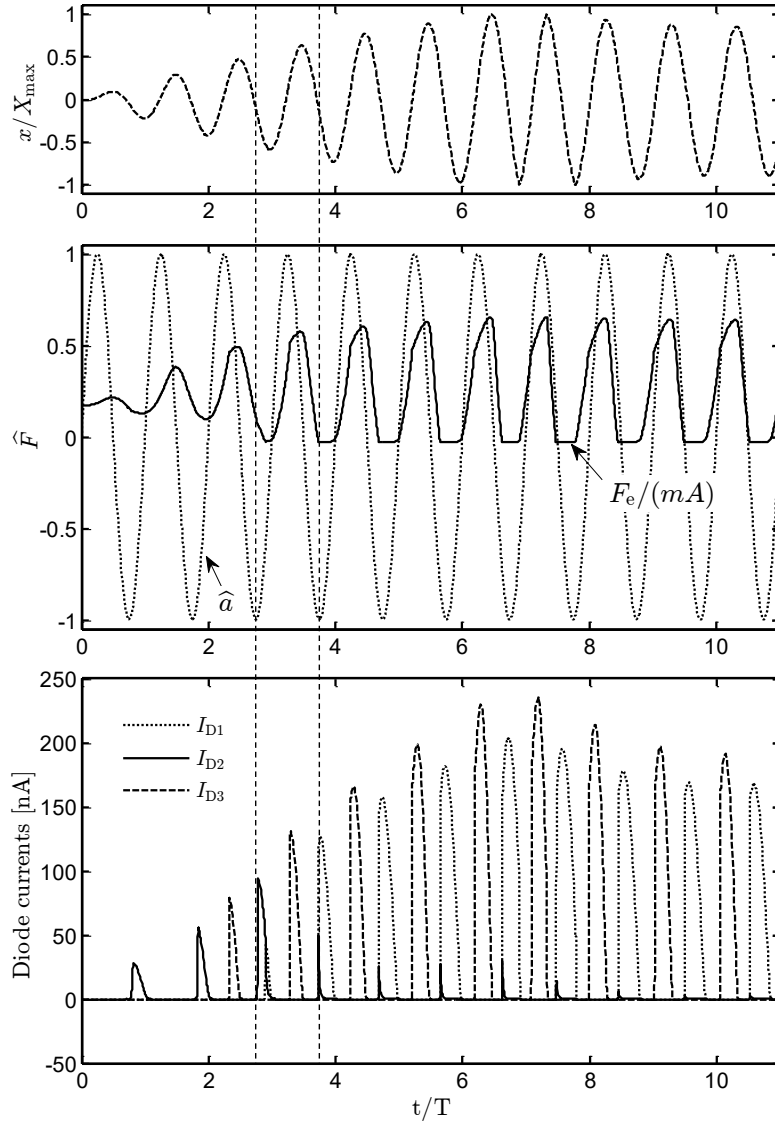
(A) Mathematically idealized diode.
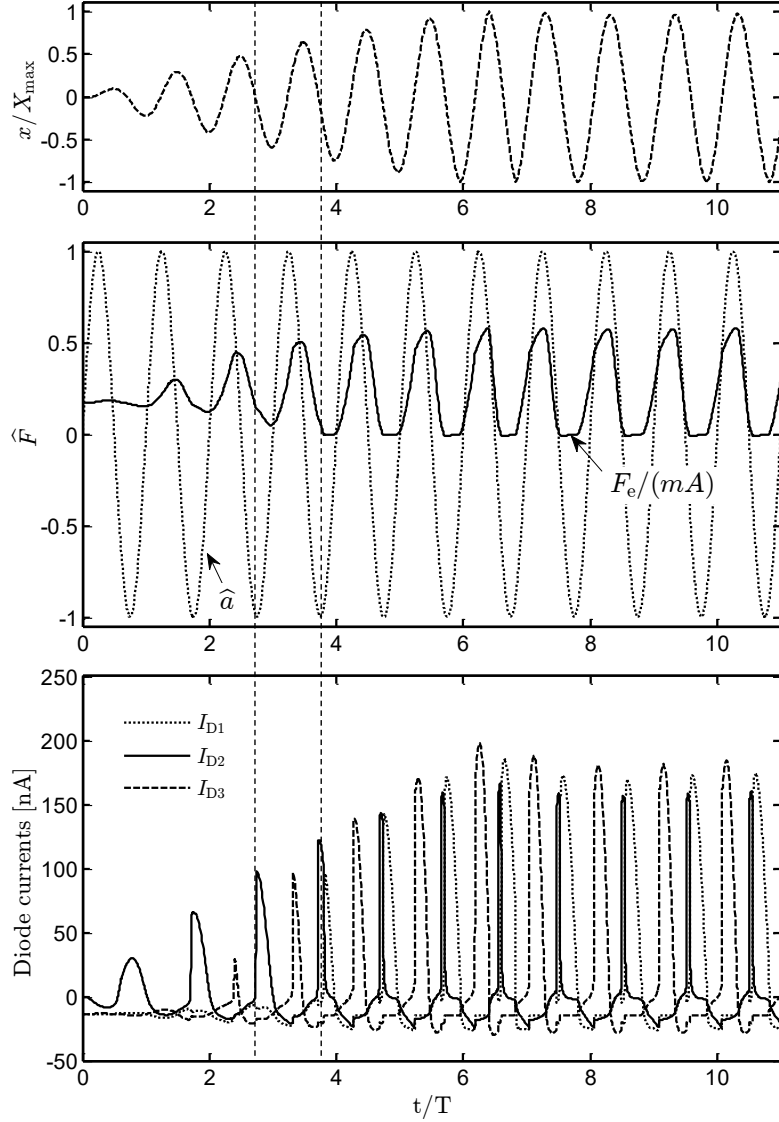
(B) Diode 1N6263.

FIGURE 10. Waveforms of normalized displacement, vibrational excitation, electrostatic force and currents through diodes D_1, D_2 and D_3 at the first several cycles of operation, with $A = 2.0$ g and $f = f_0$.

depends on both the transducing force and the diode operation mechanism. This statement is also valid when a realistic diode model is utilized, as seen in Figure 10b.

5. CIRCUITS TO IMPROVE THE SATURATION VOLTAGE

Analyzing Bennet's doubler circuit operation, we realize that there are several promising techniques to enhance the saturation voltage with the same harvester. The main objectives of this section are to introduce and study these alternative configurations. The Q–V cycle is still a useful tool to explore some important properties of the saturation voltage under certain conditions.

5.1. **An alternative voltage doubler with single switch.** The diode D_1 plays a vital role in initially charging C_1. However, in principle, it could be removed after a few transient vibration
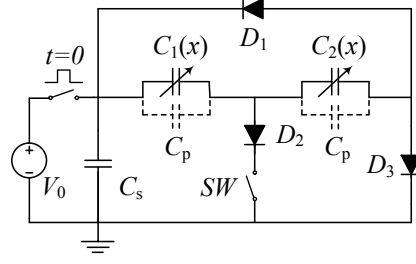
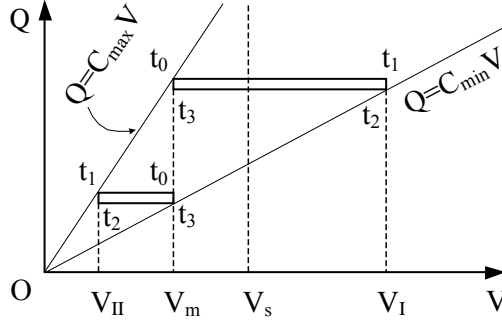FIGURE 11. An alternative topology with single switch connected in series with the diode D_2.

FIGURE 12. Q–V diagram of Bennet's doubler at the steady–state for both variable capacitors when the switch SW is added.

TABLE 3. Model parameters of SW. R_{on} – On resistance, R_{off} – Off resistance.

SW	R_{on} [Ω]	R_{off} [Ω]
Lossless	1e-3	1e12
Lossy	2	1e9

cycles without causing negative effects on the operation of the circuit. Disconnecting D_2 also enhances the charging current through the storage capacitor due to the relation $I_{\text{Cs}} = I_{\text{D3}} - I_{\text{D2}}$. The performance of the harvester, in this case, becomes of interest to investigate.

As shown in Figure 11, an electronic switch SW in series with D_2 is utilized to disconnect this diode when needed. With the use of mathematically–ideal diodes, the operation of the circuit can be described by two rectangular Q–V cycles as in Figure 12. The only constraint of V_{s} extracted from the Q–V diagram is $V_{\text{m}} \leq V_{\text{s}} \leq V_{\text{I}}$, where V_{m} and V_{I} are the minimum and maximum voltages across the capacitor $C_1(x)$. Any value of $V_{\text{s}} \in [V_{\text{m}}, V_{\text{I}}]$ satisfies the circuit operation. Thus, V_{s} cannot be solved for an explicit form of system parameters (e.g., C_0, C_{p}, and b) and input excitation. However, based on the fact that the displacement at the steady–state is limited, $X_{\text{s}} \leq X_{\text{max}}$, the maximum possible saturation voltage is estimated as

$$(5.1) \qquad {}^{\max}V_{\text{s}} = \begin{cases} mA\sqrt{\dfrac{2}{(C_0 + C_{\text{p}})b\omega_0}}, & \text{if } 0 < \dfrac{mA}{2x_0 b\omega_0} \leq \dfrac{X_{\text{max}}}{x_0} \\[4mm] 2\sqrt{2}\sqrt{\dfrac{X_{\text{max}}(mA - X_{\text{max}}b\omega_0)}{C_0 + C_{\text{p}}}}, & \text{otherwise.} \end{cases}$$

The detailed analysis is shown in the Appendix D.
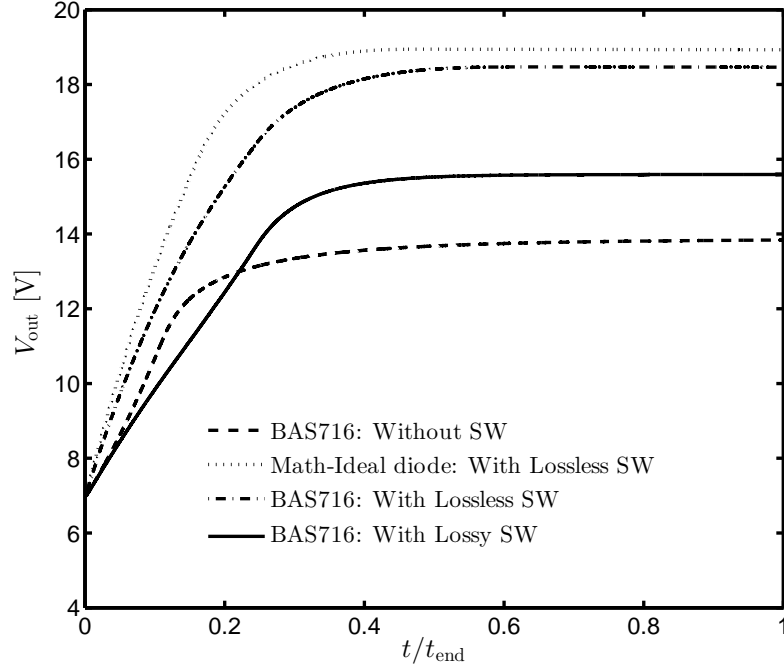
(A) $A = 2$ g
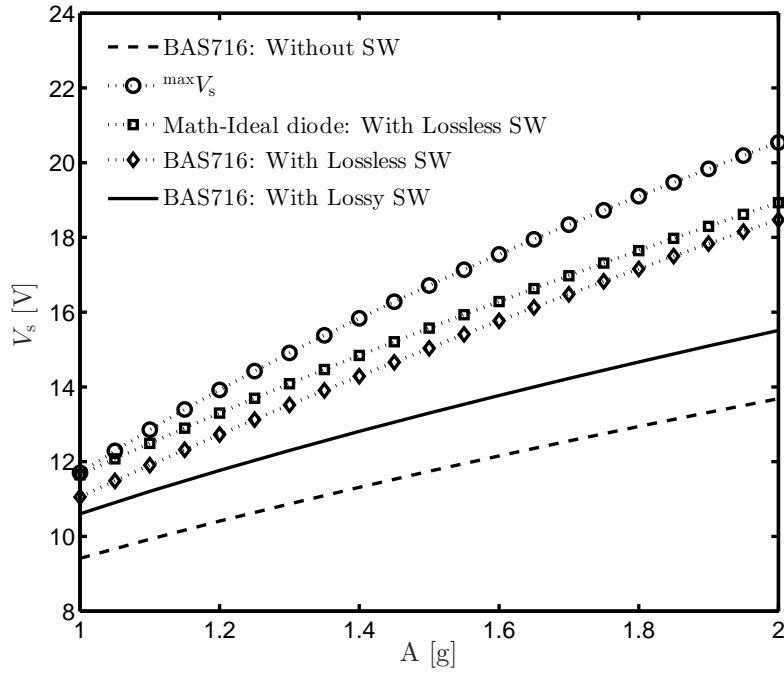
(B) Acceleration responses

FIGURE 13. Comparison of different cases without/with lossless/with lossy switch:
(a) The time evolution of output voltage at $A = 2$ g, and (b) The saturation voltage
versus acceleration amplitudes.

In the simulation, switch SW is only ON in the first several vibration cycles. It then is turned
OFF to eliminate the effect of D_2 on I_{Cs}. Two different models representing so–called lossless (or
low–loss) and lossy SW are utilized with the model parameters listed in Table 3. Figure 13a shows
the evolution of the output voltage in various cases, including without and with the presence of

lossy SW. The saturation voltage in the latter case is about ~ 15.60 V, a significant improvement over the 13.84 V achieved for the circuit topology in Figure 2. As expected, the output voltage is further increased when the power loss of the switch is neglected and an ideal switch model is used. Similar results are obtained with different acceleration amplitudes in Figure 13b. In comparison with dynamic simulations, $^{\max}V_s$ obtained from expression (5.1) is higher since the steady–state displacement X_s in the analytical solution is assumed to attain its maximum possible value (see Appendix D). The corresponding displacement in LTspice simulation may not reach this maximum with the given harvester parameters.

5.2. **Cockcroft-Walton generator applied to MEMS device.** Another topology of the voltage doubler developed from the Greinacher circuit [30] is depicted in Figure 14, in which the feedback diode D_2 is added to connect the storage capacitor and the two transducers. *Both theoretical operation analysis and simulation results show that the performances of Bennet's doubler and the Greinacher configuration are identical.* The roles of the three diodes D_1, D_2, and D_3 are the same as those in Figure 2.

Based on the Greinacher doubler circuit, a well–known voltage cascade was early proposed by the British and Irish physicists John D. Cockcroft and Ernest T. S. Walton in 1932 [31, 32]. The Cockcroft–Walton generator (named after the two authors) was proven to be able to generate a high DC output voltage from a low AC input voltage, which is hence interesting to be utilized for micro–scale harvesters. Figure 15 shows the circuit diagram of the two–stage Cockcroft–Walton generator, in which the voltage across two capacitors C_{s1} and C_{s3} is the output voltage, denoted as V_{out}. The simplified operation of such a multi–stage voltage doubler is depicted in Figure 16. Similar to Bennett's configuration, the operation of the Cockcroft–Walton multiplier can also be divided into
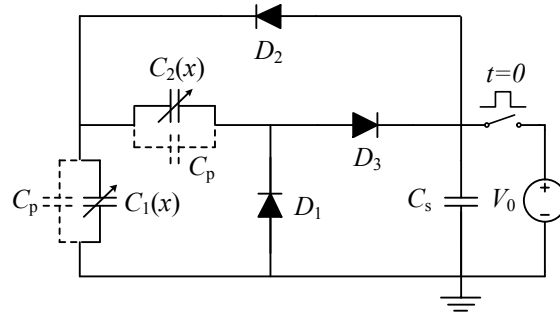

FIGURE 14. An adapted configuration of the Greinacher's doubler.
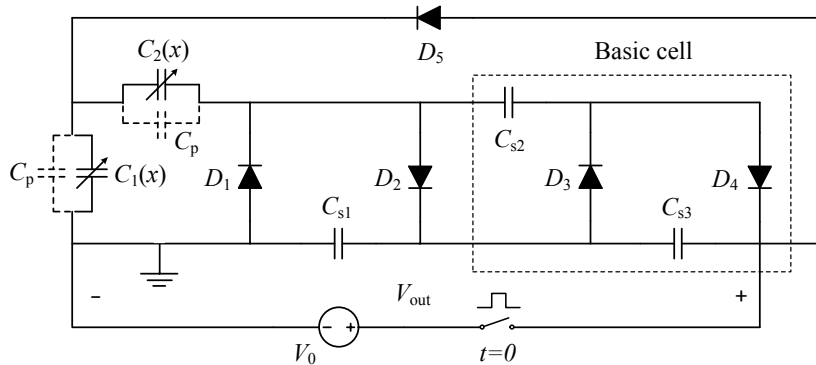
FIGURE 15. Two–stage Cockcroft-Walton multiplier.
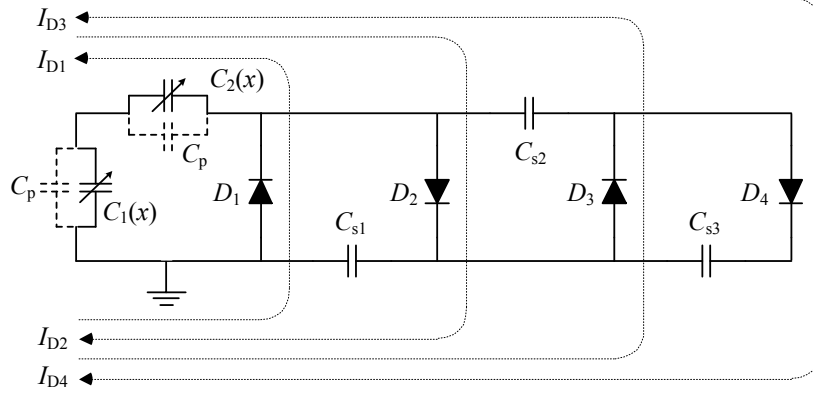
FIGURE 16. Main operation of the two-stage Cockcroft-Walton multiplier.
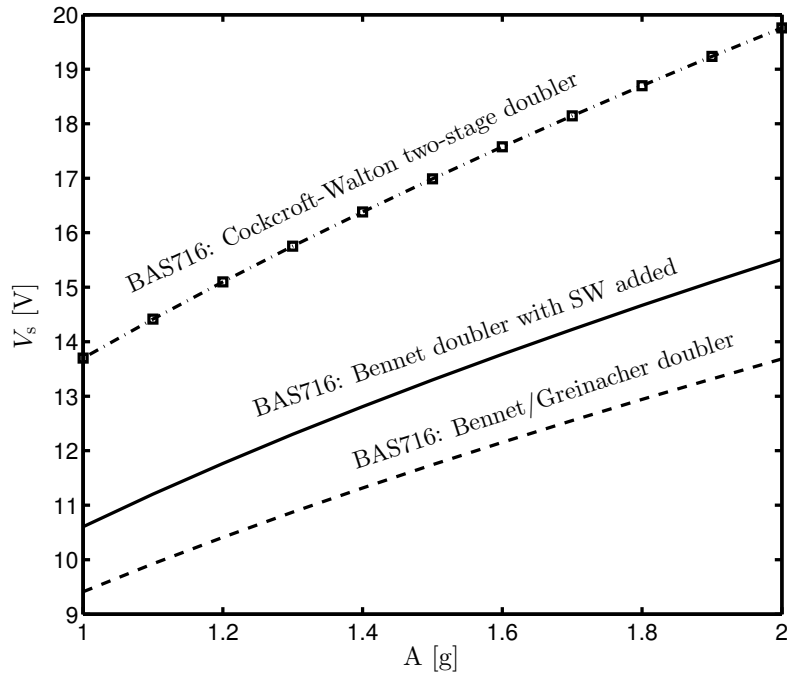
FIGURE 17. Comparison of the saturation voltage versus acceleration amplitude for the Bennet's doubler and the two-stage Cockcroft-Walton voltage multiplier.

a sequence of four stages. At first, all diodes are blocked. In the second stage, D_1 and D_3 are simultaneously conducting, and the charges are transferred to C_2 and C_{s2}. All diodes are reverse–biased and blocked in the third stage. In the final stage, D_2 and D_4 are conducting, transferring the scavenged energy to C_{s1} and C_{s3}. D_5 is mainly used to pre–charge C_1, and its conduction during operation is insignificant and disregarded. In principle, the steady–state operation of these stages can also be approximately described by a rectangular Q–V diagram. However, the relations between voltages at circuit nodes and diode states (ON/OFF) of such a multiplier are much more complicated than that of Bennet's doubler. Therefore, the analytical derivation of the saturation voltage is still left as an open question.

Figure 17 shows a substantial increase of the saturation voltage when the Cockcroft-Walton multiplier and the Bennet's doubler are compared. Since the topology discussed in Section 5.1 requires a control unit for controlling the switch, the Cockcroft–Walton multiplier may be more

convenient to keep the simplicity of the energy harvesting system in practical implementation. More importantly, our simulations reveal that, unlike Bennet's doubler, the Cockcroft–Walton circuit topology can operate with a low ratio of capacitance variation. In particular, the lowest capacitance ratio is found as $\eta_{\mathrm{min}} = 1.52$, making such a circuit attractive for further investigation in future work.

6. Conclusion

This article presented a theoretical analysis of MEMS electrostatic energy harvesters configured as Bennet's doubler, particularly at the saturation regime. The study is based on the combination of Q–V diagrams and dynamic simulations. The steady–state operation of the voltage doubler circuit was approximated by a right–angled trapezoidal conversion cycle. The use of mathematically idealized and non–ideal diode models was investigated, resulting in different analytical solutions for the saturation voltages. The theoretical approach was verified by circuit simulation results obtained from a complete model of the energy harvesting system. We discussed the effects of the diode operation mechanism on an important behavior of the system, in which the input mechanical vibration and the electrostatic force are in–phase. A similarity between Bennet's doubler and the resistive flyback charge pump circuit was highlighted by comparing their Q–V diagram. A variation circuit of Bennet's doubler with a single switch was introduced, where the saturation voltage was significantly improved in comparison with the conventional configuration. Cockcroft-Walton multiplier is another promising alternative since it shows the potential to work with MEMS harvesters that have a small varying capacitance ratio.

Appendix A. Derivation of X_{s}, V_{I} and V_{II} in Section 2

Equation (2.6) is rewritten as

$$(A.1) \qquad \frac{1 + \dfrac{C_0}{C_{\mathrm{p}}}\left(1 + \dfrac{X_{\mathrm{s}}}{x_0}\right)}{1 + \dfrac{C_0}{C_{\mathrm{p}}}\left(1 - \dfrac{X_{\mathrm{s}}}{x_0}\right)} = \frac{2\left(1 + \dfrac{C_0}{C_{\mathrm{p}}}\right)}{1 + \dfrac{C_0}{C_{\mathrm{p}}}\left(1 + \dfrac{X_{\mathrm{s}}}{x_0}\right)}$$

$$(A.2) \qquad \Longleftrightarrow \left(1 + \frac{C_0}{C_{\mathrm{p}}} + \frac{C_0}{C_{\mathrm{p}}}\frac{X_{\mathrm{s}}}{x_0}\right)^2 = 2\left(1 + \frac{C_0}{C_{\mathrm{p}}} - \frac{C_0}{C_{\mathrm{p}}}\frac{X_{\mathrm{s}}}{x_0}\right)\left(1 + \frac{C_0}{C_{\mathrm{p}}}\right)$$

$$(A.3) \qquad \Longleftrightarrow \left(\frac{C_0}{C_{\mathrm{p}}}\frac{X_{\mathrm{s}}}{x_0}\right)^2 + 4\left(1 + \frac{C_0}{C_{\mathrm{p}}}\right)\left(\frac{C_0}{C_{\mathrm{p}}}\frac{X_{\mathrm{s}}}{x_0}\right) - \left(1 + \frac{C_0}{C_{\mathrm{p}}}\right)^2 = 0.$$

One solution of (A.3) is

$$(A.4) \qquad \left(\frac{C_0}{C_{\mathrm{p}}}\frac{X_{\mathrm{s}}}{x_0}\right) = \left(-\sqrt{5} - 2\right)\left(1 + \frac{C_0}{C_{\mathrm{p}}}\right) < 0,$$

and therefore is eliminated. The positive solution is

$$(A.5) \qquad \left(\frac{C_0}{C_{\mathrm{p}}}\frac{X_{\mathrm{s}}}{x_0}\right) = \left(\sqrt{5} - 2\right)\left(1 + \frac{C_0}{C_{\mathrm{p}}}\right)$$

$$(A.6) \qquad \Longleftrightarrow \frac{X_{\mathrm{s}}}{x_0} = \left(\sqrt{5} - 2\right)\left(1 + \frac{C_{\mathrm{p}}}{C_0}\right).$$

Substituting (A.5) into (2.4) along with $x(t_1) = X_\mathrm{s}$, we get

(A.7)
$$V_\mathrm{I} = V_1(t_1) = V_\mathrm{s}\frac{1 + \frac{C_0}{C_\mathrm{p}}\left(1 + \frac{X_\mathrm{s}}{x_0}\right)}{1 + \frac{C_0}{C_\mathrm{p}}\left(1 - \frac{X_\mathrm{s}}{x_0}\right)} = V_\mathrm{s}\frac{\left(1 + \frac{C_0}{C_\mathrm{p}}\right) + \left(\sqrt{5} - 2\right)\left(\frac{C_0}{C_\mathrm{p}} + 1\right)}{\left(1 + \frac{C_0}{C_\mathrm{p}}\right) - \left(\sqrt{5} - 2\right)\left(\frac{C_0}{C_\mathrm{p}} + 1\right)}$$
$$= V_\mathrm{s}\frac{\left(\sqrt{5} - 2\right)\left(1 + \frac{C_0}{C_\mathrm{p}}\right)}{\left(3 - \sqrt{5}\right)\left(1 + \frac{C_0}{C_\mathrm{p}}\right)} = V_\mathrm{s}\frac{\sqrt{5} + 1}{2}.$$

The solution of V_II is then

(A.8)
$$V_\mathrm{II} = V_\mathrm{I} - V_\mathrm{s} = V_\mathrm{s}\frac{\sqrt{5} - 1}{2}.$$

APPENDIX B. DERIVATION OF V_s IN SECTION 3

From (3.10), F_0 can be expressed as

(B.1)
$$F_0 = mA - X_\mathrm{s}b\omega_0.$$

Substituting X_s and F_0 from (2.7) and (3.6), respectively, into (B.1), we have that

(B.2)
$$\frac{2 + \sqrt{5}}{8}\frac{C_0}{x_0}V_\mathrm{s}^2 = mA - \left(\sqrt{5} - 2\right)\left(1 + \frac{C_\mathrm{p}}{C_0}\right)x_0b\omega_0,$$

which results in the closed form of V_s in (3.11).

APPENDIX C. DERIVATION OF X_s, x_1, V_I AND V_II IN SECTION 4

Equation (4.10) is equivalent to

(C.1)
$$\frac{1 + \frac{C_0}{C_\mathrm{p}}}{1 + \frac{C_0}{C_\mathrm{p}}\left(1 - \frac{X_\mathrm{s}}{x_0}\right)} = \frac{2\left(1 + \frac{C_0}{C_\mathrm{p}}\right) + \frac{C_0}{C_\mathrm{p}}\frac{X_\mathrm{s}}{x_0}}{1 + \frac{C_0}{C_\mathrm{p}}\left(1 + \frac{X_\mathrm{s}}{x_0}\right)}$$

(C.2)
$$\Longleftrightarrow \left(1 + \frac{C_0}{C_\mathrm{p}}\right)\left[1 + \frac{C_0}{C_\mathrm{p}}\left(1 + \frac{X_\mathrm{s}}{x_0}\right)\right] = \left[1 + \frac{C_0}{C_\mathrm{p}}\left(1 - \frac{X_\mathrm{s}}{x_0}\right)\right]\left[2\left(1 + \frac{C_0}{C_\mathrm{p}}\right) + \frac{C_0}{C_\mathrm{p}}\frac{X_\mathrm{s}}{x_0}\right]$$

(C.3)
$$\Longleftrightarrow \left(1 + \frac{C_0}{C_\mathrm{p}}\right)^2 - 2\frac{C_0}{C_\mathrm{p}}\frac{X_\mathrm{s}}{x_0}\left(1 + \frac{C_0}{C_\mathrm{p}}\right) - \left(\frac{C_0}{C_\mathrm{p}}\frac{X_\mathrm{s}}{x_0}\right)^2 = 0.$$

Similarly, the positive solution of (C.3) is

(C.4)
$$1 + \frac{C_0}{C_\mathrm{p}} = (\sqrt{2} + 1)\frac{C_0}{C_\mathrm{p}}\frac{X_\mathrm{s}}{x_0}$$

(C.5)
$$\Longleftrightarrow \frac{X_\mathrm{s}}{x_0} = (\sqrt{2} - 1)\left(1 + \frac{C_\mathrm{p}}{C_0}\right).$$

Substituting (C.5) into (4.1), we have

(C.6)
$$\left(3 - 2\sqrt{2}\right)\left(1 + \frac{C_0}{C_\mathrm{p}}\right)^2 - 2\frac{C_0}{C_\mathrm{p}}\frac{x_1}{x_0}\left(1 + \frac{C_0}{C_\mathrm{p}}\right) - \left(\frac{C_0}{C_\mathrm{p}}\frac{x_1}{x_0}\right)^2 = 0.$$

Eliminating any negative solutions, $x_1 = x(t_1)$ is then determined by

(C.7)
$$1 + \frac{C_0}{C_\mathrm{p}} = \left(3 + 2\sqrt{2}\right)\left(\sqrt{4 - 2\sqrt{2}} + 1\right)\frac{C_0}{C_\mathrm{p}}\frac{x_1}{x_0}$$

(C.8)
$$\Longleftrightarrow \frac{x_1}{x_0} = \left(\sqrt{4 - 2\sqrt{2}} - 1\right)\left(1 + \frac{C_\mathrm{p}}{C_0}\right).$$

The closed forms of V_I and V_II are given as follows

$$(\text{C.9}) \qquad V_\mathrm{I} = V_1(t_2) = V_\mathrm{s} \frac{1 + \frac{C_0}{C_\mathrm{p}}}{1 + \frac{C_0}{C_\mathrm{p}}(1 - \frac{X_\mathrm{s}}{x_0})} = V_\mathrm{s} \frac{1 + \frac{C_0}{C_\mathrm{p}}}{(2 - \sqrt{2})(1 + \frac{C_0}{C_\mathrm{p}})} = V_\mathrm{s}\left(1 + \frac{1}{\sqrt{2}}\right),$$

$$(\text{C.10}) \qquad V_\mathrm{II} = V_2(t_1) = V_\mathrm{s} \frac{1 + \frac{C_0}{C_\mathrm{p}}(1 - \frac{X_\mathrm{s}}{x_0})}{1 + \frac{C_0}{C_\mathrm{p}}(1 + \frac{x_1}{x_0})} = V_\mathrm{s} \frac{(2 - \sqrt{2})(1 + \frac{C_0}{C_\mathrm{p}})}{\sqrt{4 - 2\sqrt{2}}(1 + \frac{C_0}{C_\mathrm{p}})} = V_\mathrm{s}\sqrt{1 - \frac{1}{\sqrt{2}}}.$$

Appendix D. A summary of the operation and derivation of the upper-bound saturation voltage in Section 5.1

With the use of the mathematically ideal diode model, the relations of charge and voltage at the saturation regime for both transducers are approximated as a rectangular in Figure 12. The Q–V cycle is very similar to that of the case presented in Section 2, except that the saturation voltage V_s is unknown and $V_\mathrm{m} \leq V_\mathrm{s} \leq V_\mathrm{II}$. All the following computations are only based on the Q–V diagram.

Stage I:

At $t = t_0$, $x(t_0) = -X_\mathrm{s}$ and $V_1(t_0) = V_2(t_0) = V_\mathrm{m}$. The charges q_1, q_2 and the voltages V_1, V_2 when $t \in [t_0, t_1]$ are expressed as follows

$$(\text{D.1}) \qquad q_1\Big|_{t \in [t_0, t_1]} = V_\mathrm{m}\left[C_\mathrm{p} + C_0(1 + \frac{X_\mathrm{s}}{x_0})\right],$$

$$(\text{D.2}) \qquad q_2\Big|_{t \in [t_0, t_1]} = V_\mathrm{m}\left[C_\mathrm{p} + C_0(1 - \frac{X_\mathrm{s}}{x_0})\right],$$

$$(\text{D.3}) \qquad V_1\Big|_{t \in [t_0, t_1]} = \frac{q_1}{C_1} = \frac{V_\mathrm{m}\left[C_\mathrm{p} + C_0(1 + \frac{X_\mathrm{s}}{x_0})\right]}{C_\mathrm{p} + C_0(1 - \frac{x}{x_0})},$$

$$(\text{D.4}) \qquad V_2\Big|_{t \in [t_0, t_1]} = \frac{q_2}{C_2} = \frac{V_\mathrm{m}\left[C_\mathrm{p} + C_0(1 - \frac{X_\mathrm{s}}{x_0})\right]}{C_\mathrm{p} + C_0(1 + \frac{x}{x_0})}.$$

Stage II:

At $t = t_1$, $x(t_1) = x_1$, $V_1(t_1) = V_\mathrm{II}$, $V_2(t_1) = V_\mathrm{I}$ and diode D_3 starts to conduct, which yields

$$(\text{D.5}) \qquad V_\mathrm{II} = V_\mathrm{s} + V_\mathrm{I}$$

$$(\text{D.6}) \qquad \Longleftrightarrow V_\mathrm{m} \frac{1 + \frac{C_0}{C_\mathrm{p}}\left(1 + \frac{X_\mathrm{s}}{x_0}\right)}{1 + \frac{C_0}{C_\mathrm{p}}\left(1 - \frac{x_1}{x_0}\right)} = V_\mathrm{s} + V_\mathrm{m} \frac{1 + \frac{C_0}{C_\mathrm{p}}\left(1 - \frac{X_\mathrm{s}}{x_0}\right)}{1 + \frac{C_0}{C_\mathrm{p}}\left(1 + \frac{x_1}{x_0}\right)}.$$

The net charge pumped from C_1 into C_2 is considered negligible $\Delta Q \approx 0$.

Stage III:

From $t_2 \longrightarrow t_3$, q_1 and q_2 are constant,

$$(\text{D.7}) \qquad q_1\Big|_{t \in [t_2, t_3]} = V_\mathrm{m}\left[C_\mathrm{p} + C_0(1 + \frac{X_\mathrm{s}}{x_0})\right] - \Delta Q \approx V_\mathrm{m}\left[C_\mathrm{p} + C_0(1 + \frac{X_\mathrm{s}}{x_0})\right],$$

$$(\text{D.8}) \qquad q_2\Big|_{t \in [t_2, t_3]} = V_\mathrm{m}\left[C_\mathrm{p} + C_0(1 - \frac{X_\mathrm{s}}{x_0})\right] + \Delta Q \approx V_\mathrm{m}\left[C_\mathrm{p} + C_0(1 - \frac{X_\mathrm{s}}{x_0})\right].$$

At $t = t_2$, $V_1(t_2) = V_1(t_1)$ and $x(t_2) = X_s$, we get

$$(D.9) \qquad V_m \frac{1 + \frac{C_0}{C_p}\left(1 + \frac{X_s}{x_0}\right)}{1 + \frac{C_0}{C_p}\left(1 - \frac{X_s}{x_0}\right)} = V_m \frac{1 + \frac{C_0}{C_p}\left(1 + \frac{X_s}{x_0}\right)}{1 + \frac{C_0}{C_p}\left(1 - \frac{x_1}{x_0}\right)}$$

$$(D.10) \qquad \Longleftrightarrow x_1 = X_s.$$

The equation (D.6) then becomes

$$(D.11) \qquad \frac{1 + \frac{C_0}{C_p}\left(1 + \frac{X_s}{x_0}\right)}{1 + \frac{C_0}{C_p}\left(1 - \frac{X_s}{x_0}\right)} = \frac{V_s}{V_m} + \frac{1 + \frac{C_0}{C_p}\left(1 - \frac{X_s}{x_0}\right)}{1 + \frac{C_0}{C_p}\left(1 + \frac{X_s}{x_0}\right)}.$$

Stage IV:

At $t = t_3$, $V_1(t_3) = V_2(t_3) = V_m$ and D_1 starts to conduct, hence

$$(D.12) \qquad V_m \frac{\left[C_p + C_0(1 + \frac{X_s}{x_0})\right]}{C_p + C_0(1 - \frac{x_3}{x_0})} = V_m \frac{\left[C_p + C_0(1 - \frac{X_s}{x_0})\right]}{C_p + C_0(1 + \frac{x_3}{x_0})} = V_m$$

$$(D.13) \qquad \Longleftrightarrow x_3 = -X_s.$$

The charge on C_1 at $t = t_4$ is

$$(D.14) \qquad q_1(t_4) \approx q_1(t_3) = V_m\left[C_p + C_0(1 + \frac{X_s}{x_0})\right] = q_1(t_0).$$

Thus, the state of the circuit at t_4 is identical to that at t_0, and a new cycle starts.

The aim of analyzing the Q–V diagram is to express V_I and V_{II} in terms of V_s for further investigation. Unfortunately, the exploration above only leads to one equation (i.e., (D.11)) for two unknowns $V_r = V_s/V_m$ and X_s, therefore such a goal cannot be done. However, due to the fact that $0 < x_r = X_s/x_0 \le X_{max}/x_0$, a closed–form expression for maximum V_s (denoted as $^{max}V_s$) as a function of transducer parameters and external input is possible.

Denote $C_0/C_p = C_r$, from equations (D.5) and (D.11), V_I, V_{II} and V_r are written as

$$(D.15) \qquad \gamma = \frac{1 + C_r + C_r x_r}{1 + C_r - C_r x_r} > 1,$$

$$(D.16) \qquad V_I = V_m \gamma,$$

$$(D.17) \qquad V_{II} = V_m \frac{1}{\gamma},$$

$$(D.18) \qquad V_r = V_m \frac{\gamma^2 - 1}{\gamma}.$$

The harmonic forms of V_1 and V_2 are then

$$(D.19) \qquad V_1 = \frac{1}{2}V_m(\gamma + 1) + \frac{1}{2}V_m(\gamma - 1)\sin(\omega t),$$

$$(D.20) \qquad V_2 = \frac{1}{2}V_m\left(\frac{1}{\gamma} + 1\right) + \frac{1}{2}V_m\left(\frac{1}{\gamma} - 1\right)\sin(\omega t),$$

resulting in

$$(D.21) \qquad V_1^2 - V_2^2 = V_m^2 \frac{(\gamma^2 - 1)(\gamma + 1)^2}{4\gamma^2}(\sin(\omega t) + 1)\left[1 + \left(\frac{\gamma - 1}{\gamma + 1}\right)^2 \sin(\omega t)\right].$$

Since $\left(\frac{\gamma-1}{\gamma+1}\right)^2 \ll 1$ is negligible, the electrostatic force is

$$F_{\mathrm{e}} = F_0(\sin(\omega t) + 1), \tag{D.22}$$

$$\text{where } F_0 = V_{\mathrm{m}}^2\left[\frac{1}{8}\frac{C_0}{x_0}\frac{(\gamma^2-1)(\gamma+1)^2}{\gamma^2}\right] = V_{\mathrm{m}}^2\beta. \tag{D.23}$$

At the resonance frequency, equations (B.1) and (D.23) imply that

$$V_{\mathrm{m}}^2\beta = mA - x_0 x_{\mathrm{r}} b\omega_0, \tag{D.24}$$

$$\implies V_{\mathrm{m}}^2 = \frac{mA - x_0 x_{\mathrm{r}} b\omega_0}{\beta}. \tag{D.25}$$

From (D.18), (D.23) and (D.25), the expression of V_{s} is determined by

$$V_{\mathrm{s}} = 2\sqrt{2}\sqrt{\frac{\gamma-1}{\gamma+1}\frac{mA - x_0 x_{\mathrm{r}} b\omega_0}{\frac{C_0}{x_0}}} = 2\sqrt{2}\sqrt{\frac{C_{\mathrm{r}} x_{\mathrm{r}}}{C_{\mathrm{r}}+1}\frac{mA - x_0 x_{\mathrm{r}} b\omega_0}{\frac{C_0}{x_0}}}. \tag{D.26}$$

The derivative of V_{s} with respect to x_{r} is

$$\frac{\partial V_{\mathrm{s}}}{\partial x_{\mathrm{r}}} = 4\frac{x_0}{C_0}\frac{C_{\mathrm{r}}}{C_{\mathrm{r}}+1}\frac{mA - 2x_0 x_{\mathrm{r}} b\omega_0}{V_{\mathrm{s}}}. \tag{D.27}$$

The optimal values of x_{r} as a function of the input acceleration is

$$^{\mathrm{opt}}x_{\mathrm{r}} = \begin{cases} \dfrac{mA}{2x_0 b\omega_0}, & \text{if } 0 < \dfrac{mA}{2x_0 b\omega_0} \leq \dfrac{X_{\max}}{x_0} \\ \dfrac{X_{\max}}{x_0}, & \text{otherwise.} \end{cases} \tag{D.28}$$

Therefore, the maximum saturation voltage is

$$^{\max}V_{\mathrm{s}} = \begin{cases} mA\sqrt{\dfrac{2}{(C_0+C_{\mathrm{p}})b\omega_0}}, & \text{if } 0 < \dfrac{mA}{2x_0 b\omega_0} \leq \dfrac{X_{\max}}{x_0} \\ 2\sqrt{2}\sqrt{\dfrac{X_{\max}(mA - X_{\max} b\omega_0)}{C_0+C_{\mathrm{p}}}}, & \text{otherwise.} \end{cases} \tag{D.29}$$

References

[1] C. Sergiou, P. Antoniou, and V. Vassiliou, "A comprehensive survey of congestion control protocols in wireless sensor networks," *IEEE Communications Surveys Tutorials*, vol. 16, pp. 1839–1859, Fourthquarter 2014.

[2] I. Khan, F. Belqasmi, R. Glitho, N. Crespi, M. Morrow, and P. Polakos, "Wireless sensor network virtualization: A survey," *IEEE Communications Surveys Tutorials*, vol. 18, pp. 553–576, Firstquarter 2016.

[3] N. E. duToit, B. L. Wardle, and S. G. Kim, "Design considerations for MEMS-scale piezoelectric mechanical vibration energy harvesters," *Integrated Ferroelectrics*, vol. 71, pp. 121–160, July 2005.

[4] Beeby, Torah, Tudor, Glynne-Jones, O'Donnell, Saha, and Roy, "A micro electromagnetic generator for vibration energy harvesting," *Journal of Micromechanics and Microengineering*, vol. 17, no. 7, pp. 1257–1265, 2007.

[5] Y. Chiu, C.-T. Kuo, and Y.-S. Chu, "MEMS design and fabrication of an electrostatic vibration-to-electricity energy converter," *Microsystem Technologies*, vol. 13, no. 11, pp. 1663–1669, 2007.

[6] S. Roundy, P. K. Wright, and J. Rabaey, "A study of low level vibrations as a power source for wireless sensor nodes," *Computer Communications*, vol. 26, pp. 1131–1144, July 2003.

[7] V. P. Dragunov and D. I. Ostertak, "Microelectromechanical converters," *Russian Microelectronics*, vol. 41, no. 2, pp. 107–121, 2012.

[8] B. C. Yen and J. H. Lang, "A variable-capacitance vibration-to-electric energy harvester," *IEEE Transactions on Circuits and Systems—Part I: Regular Papers*, vol. 53, pp. 288–295, Feb. 2006.

[9] P. D. Mitcheson, T. C. Green, and E. M. Yeatman, "Power processing circuits for electromagnetic, electrostatic and piezoelectric inertial energy scavengers," *Microsystem Technologies*, vol. 13, no. 11, pp. 1629–1635, 2007.

[10] A. Bennet and R. Kaye, "An account of a doubler of electricity, or a machine by which the least conceivable quantity of positive or negative electricity may be continually doubled, till it becomes perceptible by common electrometers, or visible in sparks. by the Rev. Abraham Bennet, M. A.; communicated by the Rev. Richard Kaye, LL. D. F. R. S.," *Philosophical Transactions of the Royal Society of London*, vol. 77, pp. 288–296, 1787.

[11] A. C. M. de Queiroz and M. Domingues, "Electrostatic energy harvesting using doublers of electricity," in *Circuits and Systems (MWSCAS), 2011 IEEE 54th International Midwest Symposium on*, pp. 1–4, Aug 2011.

[12] A. C. M. de Queiroz and M. Domingues, "The doubler of electricity used as battery charger," *IEEE Transactions on Circuits and Systems II: Express Briefs*, vol. 58, pp. 797–801, Dec 2011.

[13] A. C. M. de Queiroz and M. Domingues, "Analysis of the doubler of electricity considering a resistive load," in *Circuits and Systems (MWSCAS), 2013 IEEE 56th International Midwest Symposium on*, pp. 45–48, Aug 2013.

[14] V. Dragunov and V. Dorzhiev, "Electrostatic vibration energy harvester with increased charging current," *Journal of Physics: Conference Series*, vol. 476, no. 1, p. 012115, 2013.

[15] E. Lefeuvre, S. Risquez, J. Wei, M. Woytasik, and F. Parrain, "Self-biased inductor-less interface circuit for electret-free electrostatic energy harvesters," *Journal of Physics: Conference Series*, vol. 557, no. 1, p. 012052, 2014.

[16] V. Dorzhiev, A. Karami, P. Basset, F. Marty, V. Dragunov, and D. Galayko, "Electret-free micromachined silicon electrostatic vibration energy harvester with the bennet 's doubler as conditioning circuit," *IEEE Electron Device Letters*, vol. 36, pp. 183–185, Feb 2015.

[17] E. Lefeuvre, J. Wei, H. Mathias, and F. Costa, "Single-switch inductorless power management circuit for electrostatic vibration energy harvesters," in *New Circuits and Systems Conference (NEWCAS), 2015 IEEE 13th International*, pp. 1–4, June 2015.

[18] C. P. Le and E. Halvorsen, "MEMS electrostatic influence machines," *Journal of Physics: Conference Series*, vol. 773, p. 012048, nov 2016.

[19] B. D. Truong, C. P. Le, and E. Halvorsen, "Analysis of electrostatic energy harvesters electrically configured as Bennet doublers," *IEEE Sensors Journal*, vol. 17, pp. 5180–5191, Aug 2017.

[20] B. D. Truong, C. P. Le, and E. Halvorsen, "Analysis of mems electrostatic energy harvesters electrically configured as voltage multipliers," *AEU - International Journal of Electronics and Communications*, vol. 107, pp. 125–136, 2019.

[21] D. Galayko, *Conditioning Circuits for Capacitive Energy Harvesters*, pp. 239–277. Cham: Springer International Publishing, 2016.

[22] D. Galayko, A. Dudka, A. Karami, E. O'Riordan, E. Blokhina, O. Feely, and P. Basset, "Capacitive energy conversion with circuits implementing a rectangular charge-voltage cycle; part 1: Analysis of the electrical domain," *IEEE Transactions on Circuits and Systems I: Regular Papers*, vol. 62, pp. 2652–2663, Nov 2015.

[23] E. O'Riordan, A. Dudka, D. Galayko, P. Basset, O. Feely, and E. Blokhina, "Capacitive energy conversion with circuits implementing a rectangular charge-voltage cycle part 2: Electromechanical and nonlinear analysis," *IEEE Transactions on Circuits and Systems I: Regular Papers*, vol. 62, pp. 2664–2673, Nov 2015.

[24] C. P. Le and E. Halvorsen, "Mems electrostatic energy harvesters with end-stop effects," *Journal of Micromechanics and Microengineering*, vol. 22, no. 7, p. 074013, 2012.

[25] S. G. Burrow, P. D. Mitcheson, and B. H. Stark, *Power Conditioning Techniques for Energy Harvesting*, pp. 323–343. New York, NY: Springer New York, 2013.

[26] S. G. Burrow and P. D. Mitcheson, *Power Conditioning for Energy Harvesting - Theory and Architecture*, pp. 85–101. Wiley-VCH Verlag GmbH & Co. KGaA, 2015.

[27] H. R. Florentino, D. Galayko, R. C. S. Freire, B. A. Luciano, and C. Florentino, "Energy Harvesting Circuit Using Variable Capacitor with Higher Performance," *Journal of Integrated Circuits and Systems*, vol. 6, no. 1, pp. 68–74, 2011.

[28] M. H. Bao, *Micro Mechanical Transducers Pressure Sensors, Accelerometers and Gyroscopes*, vol. 8 of *Handbook of Sensos and Actuators*. Elsevier, 2000.

[29] D. V. Pavlovich and D. V. Yuryevich, "Influence of diodes parameters on the operation of e-veh circuit based on bennet's doubler," *PROCEEDINGS OF THE RUSSIAN HIGHER SCHOOL ACADEMY OF SCIENCES*, vol. 31, no. 2, 2015.

[30] W. Hauschild and E. Lemke, *High-Voltage Test and Measuring Techniques*. Springer-Verlag Berlin Heidelberg, 1 ed., 2014.

[31] J. D. Cockcroft and E. T. S. Walton, "Experiments with high velocity positive ions. (i) further developments in the method of obtaining high velocity positive ions," *Proceedings of the Royal Society of London A: Mathematical, Physical and Engineering Sciences*, vol. 136, no. 830, pp. 619–630, 1932.

[32] J. D. Cockcroft and E. T. S. Walton, "Experiments with high velocity positive ions. ii. the disintegration of elements by high velocity protons," *Proceedings of the Royal Society of London A: Mathematical, Physical and Engineering Sciences*, vol. 137, no. 831, pp. 229–242, 1932.

DEPARTMENT OF MICROSYSTEMS, UNIVERSITY COLLEGE OF SOUTHEAST NORWAY, CAMPUS VESTFOLD, RAVEIEN 215, N-3184 BORRE, NORWAY. EMAIL: BINH.TRUONG@USN.NO